

Resolution doubling in live, multicellular organisms via multifocal structured illumination microscopy

Andrew G York¹, Sapun H Parekh^{1,5}, Damian Dalle Nogare², Robert S Fischer³, Kelsey Temprine¹, Marina Mione⁴, Ajay B Chitnis², Christian A Combs³ & Hari Shroff¹

We demonstrate three-dimensional (3D) super-resolution in live multicellular organisms using structured illumination microscopy (SIM). Sparse multifocal illumination patterns generated by a digital micromirror device (DMD) allowed us to physically reject out-of-focus light, enabling 3D subdiffraction imaging in samples eightfold thicker than had been previously imaged with SIM. We imaged samples at one 2D image per second, at resolutions as low as 145 nm laterally and 400 nm axially. In addition to dual-labeled, whole fixed cells, we imaged GFP-labeled microtubules in live transgenic zebrafish embryos at depths >45 μm . We captured dynamic changes in the zebrafish lateral line primordium and observed interactions between myosin IIA and F-actin in cells encapsulated in collagen gels, obtaining two-color 4D super-resolution data sets spanning tens of time points and minutes without apparent phototoxicity. Our method uses commercially available parts and open-source software and is simpler than existing SIM implementations, allowing easy integration with wide-field microscopes.

The 100-fold mismatch in size between the resolution of an optical microscope and the length scales of biomolecular complexes hinders direct observation of subcellular phenomena. Imaging beyond the diffraction limit is thus of great practical interest in cell biology, and the last decade has seen an explosion in ‘super-resolution’ optical imaging techniques¹. Despite these advances, long-term live imaging of thick samples still presents challenges for such methods.

Photoactivated localization microscopy (PALM)² and related single-molecule imaging techniques^{3,4} enable imaging with lateral resolutions down to 20 nm (sub-100 nm axially) on 3D samples such as whole fixed cells^{5,6} and much thicker cellular spheroids⁷. Although a few live-cell experiments have been performed at slow imaging rates over extended durations⁸ and at rates up to 2 Hz for very short periods⁹, the current requirements for kilowatts per square centimeter excitation intensities and thousands of frames have confined most efforts to fixed cells.

Stimulated emission depletion¹⁰ (STED) microscopy enables cellular imaging with ~20–100 nm resolution¹¹. STED microscopy has also been applied to thicker samples^{12,13}, although so far only providing 2D super-resolution. STED resolution scales with illumination intensity, constraining the choice of dyes and entailing a compromise between spatial resolution and phototoxicity in live-cell experiments.

In SIM^{14,15}, spatially patterned light is used to excite sample fluorescence. Frequency-mixing between the excitation pattern and fluorophore density moves normally unobservable high-resolution information in the sample into the observable passband of the microscope. By varying the pattern orientation and phase, recording the resulting fluorescence and appropriately processing the resulting multi-image data sets, it is possible to obtain images with ~100 nm lateral and ~300 nm axial resolution¹⁶ for linear SIM. Although this resolution is more modest than that of PALM or STED microscopy, SIM offers other advantages. The number of raw images required for a single SIM image is far fewer than in PALM, and the illumination intensity is far less than in STED microscopy. These benefits allow increased imaging speed and duration and enable live SIM at 11 Hz in two dimensions¹⁷ and 0.2 Hz in three dimensions on whole cells¹⁸ for hundreds of time points. Linear SIM is also compatible with the full array of conventional fluorescent dyes, unlike PALM or STED microscopy.

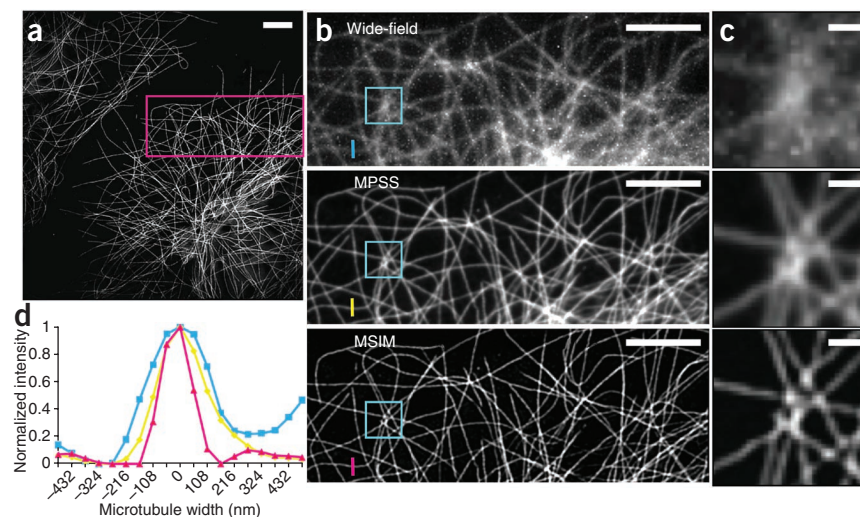
In addition to doubling resolution, 3D SIM offers another major advantage over conventional wide-field imaging: computational optical sectioning (the removal of out-of-focus blur). Although highly effective on thin samples, SIM retains the shot noise associated with the computationally removed background and is unsuitable for thick or very densely labeled samples. Confocal microscopy physically rejects out-of-focus light with a pinhole and provides higher-contrast images for thick samples. Confocal microscopes, however, provide at best a $\sqrt{2}$ improvement in lateral resolution with a small pinhole, and this enhanced resolution is difficult to attain as the corresponding loss in signal is prohibitive.

We present a hybrid technique, multifocal SIM (MSIM), that combines the resolution-doubling characteristics of SIM with

¹Section on High Resolution Optical Imaging, National Institute of Biomedical Imaging and Bioengineering, US National Institutes of Health (NIH), Bethesda, Maryland, USA. ²National Institute of Child Health and Human Development, NIH, Bethesda, Maryland, USA. ³National Heart, Lung, and Blood Institute Light Microscopy Facility, NIH, Bethesda, Maryland, USA. ⁴Institute of Toxicology and Genetics, Karlsruhe Institute of Technology, Karlsruhe, Germany.

⁵Present address: Molecular Spectroscopy Department, Max Planck Institute for Polymer Research, Mainz, Germany. Correspondence should be addressed to A.G.Y. (andrew.g.york@naturemethods@gmail.com).

Figure 1 | Resolution and contrast enhancement in MSIM. **(a)** MSIM image of microtubules stained with Alexa Fluor 488 in a fixed cell. The image was generated from 224 raw images, each acquired in 4.5 ms, for an acquisition time of ~1 s. Scale bar, 5 μm . **(b)** Magnification of the boxed region in **a**, showing a wide-field image (top), an MPSS image (middle) and an MPSS and deconvolved (MSIM) image (bottom). Scale bars, 5 μm . **(c)** Magnification of respective regions boxed in **b**. Scale bars, 1 μm . **(d)** Plots of intensity along the respectively colored lines in **b**. FWHM values are: wide-field, 299 nm; MPSS, 224 nm; and MSIM, 145 nm.



the physical optical sectioning of confocal microscopy. MSIM uses sparse 2D excitation patterns generated with a DMD integrated into a conventional wide-field microscope and digital processing after acquisition ('postprocessing') to obtain optically sectioned images with ~145-nm lateral and ~400-nm axial resolution at 1-Hz frame rates. Relative to existing SIM, our implementation is easier to integrate onto existing microscopes and is considerably cheaper than commercial SIM. We obtained dual-color, volumetric images of whole fixed cells and extend SIM to live samples eightfold thicker than previous experiments on whole cells. We applied 4D MSIM to study the evolution of the posterior lateral line primordium in live zebrafish embryos and also obtained multicolor, 4D super-resolution data sets on cells embedded in collagen gels.

RESULTS

Speeding up image scanning microscopy

Using point-like illumination for SIM has been explored in image scanning microscopy (ISM)¹⁹. In ISM, a focused beam excites fluorescence, which is imaged through a confocal pinhole and recorded onto a camera. The excitation beam is rastered through the sample, and an image is recorded for each position of the beam. An image with $\sqrt{2}$ improvement in spatial resolution is obtained by scaling (2 \times) and summing the raw images, a process analogous to stopping down the pinhole in confocal microscopy (Supplementary Note 1 and Supplementary Fig. 1). Deconvolution increases the ISM resolution to 150 nm laterally, a 1.63-fold improvement over the raw data.

ISM offers the sectioning capability of a confocal microscope and has better resolution and no trade-off in signal-to-noise ratio (SNR). The weakness of ISM is its speed: recording a single 2D image at each illumination location is far too slow for monitoring many live cellular processes. Covering a relatively small ~2 μm field of view at the required step size (40 nm), even at fast frame rates (100 Hz) results in a total acquisition time of 25 s. Larger fields would take proportionately more time.

We reasoned that parallelization of ISM by using a sparse lattice of excitation foci (similar to swept-field or spinning disk confocal microscopy) would dramatically increase speed. After excitation by this multifocal pattern and fluorescent readout, the multifocal pattern is translated, and this procedure is repeated until the entire field of view has been illuminated. Postprocessing (pinholing, 2 \times scaling and summing) gave a reconstructed image with better resolution and less out-of-focus haze than a wide-field image.

This reconstruction may be deconvolved to yield a resolution-doubled MSIM image (Supplementary Fig. 2, Supplementary Video 1 and Online Methods).

MSIM implementation

We chose a commercially available DMD (Supplementary Note 2) to generate and switch multifocal patterns, owing to its comparatively low cost and high switching speed (>20 kHz). Each illumination spot was created by a single DMD mirror pixel in the 'on' position. Our illumination optics demagnified each 10.8 $\mu\text{m} \times 10.8 \mu\text{m}$ DMD pixel by 90 \times to 120 nm \times 120 nm in the sample (Supplementary Fig. 3), generating illumination foci limited by diffraction and aberrations. Additional demagnification did not improve resolution but reduced excitation transmission efficiency.

We chose a periodic lattice of approximately equilateral triangles for our illumination locations because this pattern maximizes the distance between any two nearest neighbors for a given density of points (reducing cross-talk between points while minimizing the number of translations required to cover the field). We translated this multifocal pattern by one DMD pixel at a time, corresponding to a step size of 120 nm in the sample plane. Larger steps did not evenly illuminate the sample, giving a visible striping artifact, whereas smaller steps increased acquisition time and dose with no improvement in image quality.

Multifocal excitation patterns were imaged onto the sample mounted in a commercial, inverted microscope, and a scientific-grade complementary metal-oxide semiconductor (sCMOS) camera (Supplementary Note 3) recorded one raw image per pattern position. Varying spacing between the illumination points trades acquisition speed for sectioning quality. Widely spaced foci had less cross-talk, but more patterns were required to evenly illuminate the sample. Denser foci had more cross-talk but required correspondingly fewer patterns (Supplementary Fig. 4). We found that 16-pixel horizontal and 14-pixel vertical separation between scan points gave good results in the samples we investigated. The resulting 224 raw exposures taken at 222 Hz (for our 480 pixel \times 480 pixel field of view) corresponded to a ~1 Hz super-resolution image acquisition rate. We applied pinholing, scaling, summing and deconvolution (Supplementary Note 4) after acquisition to generate MSIM images. For pinholing,

Figure 2 | Dual-color, 3D MSIM of a fixed U2OS cell. (a) x-y maximum intensity projection, displaying Alexa Fluor 488-labeled microtubules (green) and Mitotracker Red-stained mitochondria (magenta). Scale bar, 10 μm . (b) MSIM (left) and wide-field (right) slices 1.4 μm from the coverslip surface of the region boxed in a. **The same excitation dose was delivered to the sample in MSIM and wide-field mode.** Each MSIM slice was generated from 224 raw images, each acquired in 4.5 ms, for an acquisition time of ~ 1 s per slice and a volumetric acquisition time of 30 s. Scale bars, 5 μm .

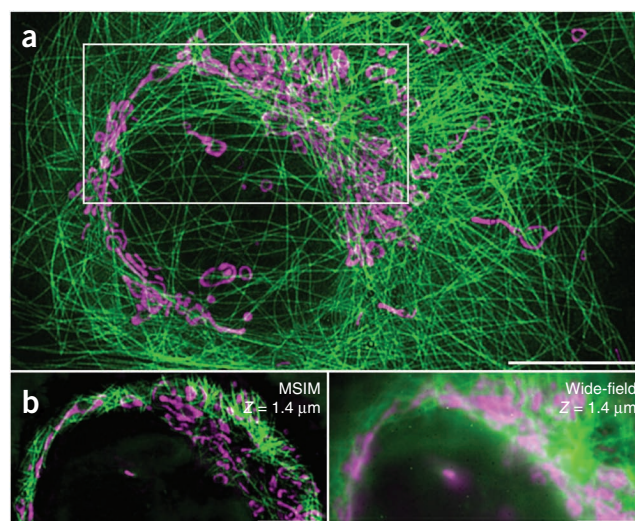
we used a Gaussian mask with $\sigma = 162$ nm centered on each illumination focus to remove out-of-focus haze (**Supplementary Fig. 5**).

Resolution doubling in biological samples

To investigate MSIM's potential for biological imaging, we imaged antibody-labeled microtubules in human osteosarcoma (U2OS) cells embedded in Fluoromount (**Fig. 1a**). Compared to wide-field images, the multifocal-excited, pinholed, scaled and summed (MPSS) images improved resolution and contrast (**Fig. 1b,c**). Iterative deconvolution additionally improved MPSS images, revealing features obscured by diffraction (**Fig. 1b,c**). The same deconvolution did not improve the resolution of wide-field images appreciably (**Supplementary Fig. 6**). The apparent full-width at half maximum (FWHM) intensity of microtubules in MSIM images was 145 nm, a twofold improvement compared to wide-field imaging (**Fig. 1d**). Similar experiments on 110-nm beads confirmed this result (MSIM FWHM of $146 \text{ nm} \pm 15 \text{ nm}$ versus wide-field FWHM of $284 \text{ nm} \pm 32 \text{ nm}$ ($\pm \text{s.d.}$), $n = 80$ beads, **Supplementary Fig. 7**). The acquisition time for the $48 \mu\text{m} \times 49 \mu\text{m}$ field (**Fig. 1a**) was ~ 1 s, more than a 6,500-fold improvement over ISM, assuming the same 222-Hz raw frame rate.

We next investigated our technique's suitability for 3D, dual-labeled samples by acquiring a z stack of MSIM images on a fixed cell embedded in Fluoromount (**Fig. 2**). We immunolabeled microtubules with Alexa Fluor 488 and stained mitochondria with Mitotracker Red, obtaining a 3- μm -thick volume with slices separated by 100 nm (**Fig. 2a** and **Supplementary Video 2**). Compared to wide-field images, 3D MSIM images had notably increased image contrast owing to the combined physical (via the digital pinholes) and computational (via 3D deconvolution) removal of out-of-focus light (**Fig. 2b** and **Supplementary Videos 2** and **3**).

MSIM images retained twofold lateral resolution improvement over wide-field imaging, better resolving microtubules and



'worm-like' mitochondria. We resolved subdiffraction voids at the ends of individual mitochondria as well as microtubule pairs separated by < 200 nm (**Supplementary Fig. 8**). Unexpectedly, MSIM improved our axial resolution $\sim 2\times$ over wide-field imaging. The apparent axial FWHM of microtubules was ~ 400 nm, a result confirmed on 110-nm beads (MSIM FWHM of $402 \text{ nm} \pm 49 \text{ nm}$ (s.d.) and wide-field imaging FWHM of $826 \text{ nm} \pm 83 \text{ nm}$, $n = 80$ beads, **Supplementary Fig. 7**).

Extension of MSIM to live, multicellular samples

Previous live SIM has been limited to axial depths of $\sim 6 \mu\text{m}$, the thickness of a single HeLa cell¹⁸. **MSIM enables 3D imaging of thicker live samples** because pinholing rejects out-of-focus light that would otherwise swamp in-focus signal. To demonstrate this feature, we imaged live, immobilized zebrafish embryos expressing a GFP transgene that labeled microtubules (**Fig. 3** and **Supplementary Videos 4** and **5**).

For MSIM of a 48.2- μm -thick volume we acquired 241 slices spaced 0.2 μm apart at a 2D imaging rate of 1 Hz (**Fig. 3a**). Although we did not measure the distance from the cover slip to the sample, five sections (1 μm thickness) were present in the stack before the first appearance of GFP signal in the epidermis of the fish. This tissue volume thus ranged from just superficial to the epidermal layer of the fish through an entire somite. Structural features, such as the boundary between two adjacent somites, alignment of microtubules along the somite boundary and microtubule-free regions corresponding to the nuclei of the developing muscle cells, are clearly visible. Estimating the axial position of nuclei suggests that the imaging volume contained 6–7 cell layers.

We imaged fast enough to capture a dividing cell in the epidermis (**Fig. 3a–c**) without substantial motion blur. The resolution enhancement of MSIM was retained throughout the volume, as the separation

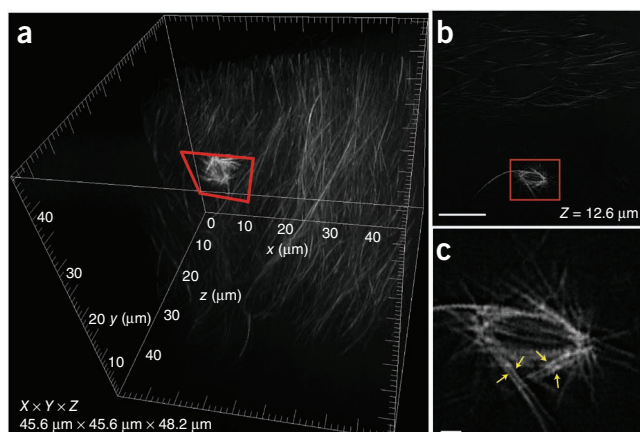
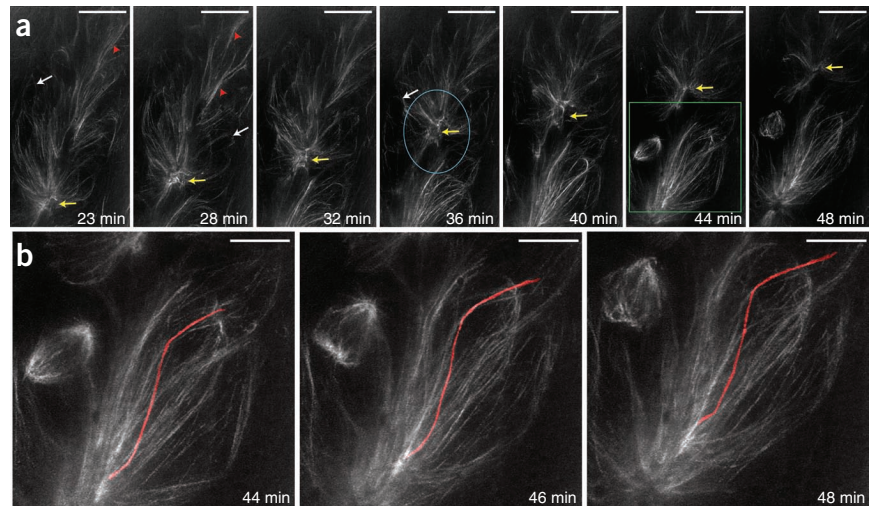


Figure 3 | 3D MSIM in a live, 24 h post-fertilization (h.p.f.) zebrafish embryo. (a) A 3D representation of the imaging volume, highlighting GFP-labeled microtubules. Red box indicates a dividing cell. (b) x-y slice 12.6 μm into the volume, emphasizing a dividing cell in the epidermis (box). Scale bar, 10 μm . (c) Higher-magnification view of the dividing cell; yellow arrows highlight features that are separated by < 200 nm. Scale bar, 1 μm . In **b,c**, the anterior direction is to the left and dorsal to the top.

Figure 4 | 4D MSIM on the posterior lateral line primordium. (a) Selected maximum intensity projections composed from the middle 18 slices of each 22-slice volume. White arrows, basal cell bodies enclosed by microtubules; yellow arrows, apical constrictions of a proto-neuromast in a rosette (outlined with a blue ellipse) as it moves toward the caudal end of the embryo; red arrowheads, groups of apical midline microtubules in the leading edge of the pLLP. Scale bars, 10 μ m. (b) Magnification of the region boxed in green in a, following a single microtubule (red) from a basal cell body to the apical constriction of a proto-neuromast through selected time points. Indicated times are relative to the initial time point of imaging. Scale bars, 5 μ m.



between microtubule pairs at the site of cell division was resolved to better than 200 nm (Fig. 3c), and microtubules in the epidermis had lateral FWHM of $175 \text{ nm} \pm 21 \text{ nm}$ ($n = 30$) and axial FWHM of $496 \text{ nm} \pm 65 \text{ nm}$ ($n = 21$). This resolution decreased to $195 \text{ nm} \pm 33 \text{ nm}$ laterally ($n = 30$) and $639 \text{ nm} \pm 88 \text{ nm}$ axially ($n = 21$) near the somite boundary (40 μ m into the stack), presumably owing to depth-dependent aberrations and scattering. Comparative experiments on a confocal microscope at similar numerical aperture (NA) and acquisition speed revealed similar features in the epidermis and somites, including individual microtubules and the nuclei of developing muscle cells (Supplementary Video 6). Although direct comparison between MSIM and confocal microscopy is difficult owing to differences in objectives, embryos, excitation power and detection efficiency, the lateral FWHM of microtubules in the epidermis was $392 \text{ nm} \pm 77 \text{ nm}$ ($n = 21$), more than $2\times$ worse than the MSIM resolution at the same depth (Supplementary Fig. 9).

Volumetric time-lapse imaging in live embryos

To explore MSIM's potential for time-lapse, volumetric (4D) imaging in multicellular organisms, we imaged the posterior lateral line primordium (pLLP)²⁰ in the same zebrafish line (Fig. 4 and Supplementary Videos 7–9). The pLLP is a group of ~ 100 cells that migrates under the epidermis along the trunk of the embryo. During migration, the pLLP periodically deposits apically constricted clusters of epithelial cells (neuromasts), which eventually form the sensory organs of the lateral line. We acquired volumetric images every minute for ~ 50 min (22 slices per volume, spaced 0.6 μ m apart, ~ 40 s between volumes), starting collection 10 μ m past the epidermis and imaging through the pLLP (Fig. 4a and Supplementary Video 7). We resolved microtubules throughout the entire pLLP, from apical neuromast constrictions to basal cell bodies, a thickness of $\sim 12 \mu$ m (Supplementary Video 8).

Of particular interest in lateral line biology is the generation and organization of proto-neuromasts in the traveling pLLP. Although much of the underlying signaling has been determined^{21,22}, the precise mechanisms by which migrating mesenchymal cells organize into centrally oriented cell clusters, or rosettes, with a prominent apical constriction remain elusive. The ability to define and follow individual microtubules (resolved to $\sim 150 \text{ nm}$) from cell bodies in the basal portion of the rosette allows precise definition of the structure of a proto-neuromast (Fig. 4a,b and Supplementary Video 9). Furthermore, the MSIM data set suggests that mesenchymal cells in the leading part of the pLLP show a prominent apical organization of microtubules at the midline of the migrating pLLP even before incorporation into a proto-neuromast (Fig. 4b). This previously undocumented feature may allow for a richer understanding of the transition that initially mesenchymal cells in the leading domain undergo as they assume an epithelial character and are incorporated into the nascent proto-neuromasts.

We also acquired 4D data sets of live, transgenic *Caenorhabditis elegans* embryos expressing GFP-labeled histones (Supplementary Fig. 10 and Supplementary Video 10). Although we recovered super-resolution information up to $\sim 10 \mu$ m, MSIM images at greater depths exhibited pronounced degradation in SNR and resolution, presumably because of increased scattering or depth-dependent aberrations induced by the sample. These deleterious effects must be addressed before super-resolution can be achieved throughout whole, live nematode embryos.

Dual-color 4D MSIM in collagen gels

Most single-cell fluorescence microscopy is performed at or near the coverslip, where imaging conditions are benign.

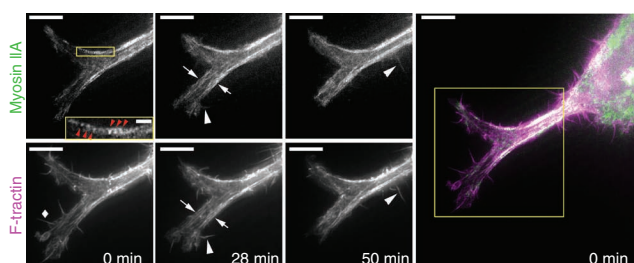


Figure 5 | Dual-color 4D MSIM in a collagen gel. Selected time point images (left), showing maximum intensity projections of invadopodium from GFP-myosin IIA and td-Tomato-F-actin channels. Scale bars, 5 μ m. Indicated times are relative to the initial time point of imaging. Highlighted are example filapodia (diamond in bottom left image); myosin striations at cell periphery (yellow inset, red arrowheads highlight 350 nm repeat frequency; scale bar, 1 μ m); actin bundles decorated with myosin (arrows); and retracting filapodia localized with myosin at base (arrowheads) are highlighted. Merged view for 0 min is shown on the right; boxed region corresponds to individual images on the left.

However, studies on breast-cancer progression²³, metastasis²⁴ and mesenchymal stem cell differentiation²⁵ show that the 3D environment of cells substantially affects their biology, highlighting the need for high-resolution methods suited for imaging away from the coverslip²⁶. We demonstrated MSIM's capability for these applications by performing multicolor 4D super-resolution imaging of human osteosarcoma cells invading a collagen matrix, more than 40 μm into the matrix (Fig. 5 and **Supplementary Video 11**). We acquired sequential two-color volumes (25 slices per volume, 0.2 μm apart, ~ 60 s between time points, 2D imaging rate 1 Hz) over 26 time points, observing interactions between myosin IIA (labeled with GFP) and actin filaments (labeled with tandem dimer (td)Tomato F-tractin) in invadopodia. Individual actin filament bundles were clearly resolved despite their close proximity (~ 250 nm) and were decorated with myosin IIA. Along the actin cortex, myosin IIA formed striations with repeat frequency of ~ 350 nm, consistent with previous findings in 2D cell culture²⁷.

At the invadopodia periphery, we observed highly dynamic filopodia, with apparent diameter of ~ 150 – 200 nm, consistent with previous observations²⁸. As groups or individual filopodia retracted, concentrations of myosin IIA concomitantly appeared, suggesting that local accumulation of myosin IIA at the cortex may cause retraction of filopodia during invasion of 3D matrices. The cell dynamically protruded and retracted throughout the 50 min imaging period, suggesting that our excitation intensities did not substantially perturb the observed dynamics.

DISCUSSION

Like existing 3D SIM¹⁶, MSIM provides resolution doubling by increasing the highest spatial frequencies encoded in the raw data, followed by deconvolution. However, the absolute resolutions we report are slightly lower than existing 3D SIM, which we attribute to two factors. First, achieving the highest possible resolution relies on obtaining diffraction-limited wide-field performance before (M)SIM is applied. Although we attempted this, the wide-field point spread functions (PSFs) we measured (**Supplementary Fig. 7**) had FWHM (~ 280 nm) larger than theoretical predictions. It is customary in SIM to screen many objectives and use only the one with highest resolution. We did not do this. Furthermore, we suspect that aberration caused by warping of the dichroic in our microscope was the major cause of departure from ideal performance, as we noticed that small adjustments of the mounting screws that held the dichroic drastically altered the PSF. A thicker, stiffer dichroic may mitigate this issue. Second, the excitation patterns in previous SIM implementations concentrate energy at the very highest lateral spatial frequencies in the objective pass-band. In contrast, the multifocal excitation patterns we used contain all spatial frequencies permitted by the objective. We might thus expect line-excitation-based SIM to provide a greater SNR at high spatial frequencies than MSIM, enabling higher resolution. We note the point-like nature of our excitation pattern offers a route to even higher resolution, perhaps by exploiting the nonlinearities provided by reversible, switchable fluorescent probes²⁹.

Compared to previous SIM implementations, our system is simpler to build. We add only a DMD, a telescope and a fast camera to a conventional wide-field microscope. Our illumination path has no moving parts and is insensitive to polarization. Finally, we do not modify the illumination path for multicolor operation, unlike existing SIM implementations³⁰.

Different implementations of MSIM could improve excitation efficiency or depth penetration. The DMD we used for generating and switching patterns proved highly inefficient. Only a small fraction ($<1\%$) of the pixels were in the on state during a given raw image, wasting the majority of the excitation light. Using a microlens array in conjunction with a scanning mirror (as in swept-field confocal microscopy) would be far more efficient and would allow MSIM with existing commercial hardware. MSIM could also use multiphoton excitation, which would result in lower-resolution images, owing to the longer excitation wavelength, but would limit excitation to the focal plane, reducing out-of-plane bleaching and improving sectioning. Longer wavelengths would also result in less scattering of the excitation and greater penetration into the sample.

METHODS

Methods and any associated references are available in the [online version of the paper](#).

Note: Supplementary information is available in the online version of the paper.

ACKNOWLEDGMENTS

We thank M. Davidson (Florida State University) for the U2OS cells, Z. Bao (Sloan-Kettering Institute) for the BV24 nematode strain, K. Hazelwood for assistance with cell culture, G. Patterson for the use of his cell culture facilities, and H. Eden, P. Winter, Y. Wu and C. Waterman for feedback and suggestions on the manuscript. S.H.P. acknowledges financial support from the American Association for the Advancement of Science. This work was supported by the Intramural Research Program of the NIH National Institute of Biomedical Imaging and Bioengineering, the National Institute of Heart, Lung, and Blood and the National Institute of Child Health and Development.

AUTHOR CONTRIBUTIONS

A.G.Y. and H.S. conceived the idea. A.G.Y., S.H.P., C.A.C. and H.S. designed and built the experimental setup. A.G.Y. and S.H.P. wrote the analysis code and performed simulations. A.G.Y., S.H.P., D.D.N., R.S.F., C.A.C. and H.S. collected data. A.G.Y., S.H.P., D.D.N., R.S.F., K.T., A.B.C., C.A.C. and H.S. analyzed data. S.H.P., D.D.N., R.S.F. and K.T. prepared samples. M.M., A.B.C. and C.A.C. contributed reagents and materials. A.G.Y., S.H.P., D.D.N., R.S.F. and H.S. wrote the paper with input from all authors. H.S. designed and supervised research.

COMPETING FINANCIAL INTERESTS

The authors declare no competing financial interests.

Published online at <http://www.nature.com/doi/10.1038/nmeth.2025>.
Reprints and permissions information is available online at <http://www.nature.com/reprints/index.html>.

- Hell, S.W. Far-field optical nanoscopy. *Science* **316**, 1153–1158 (2007).
- Betzig, E. *et al.* Imaging intracellular fluorescent proteins at nanometer resolution. *Science* **313**, 1642–1645 (2006).
- Rust, M.J., Bates, M. & Zhuang, X. Sub-diffraction-limit imaging by stochastic optical reconstruction microscopy (STORM). *Nat. Methods* **3**, 793–795 (2006).
- Hess, S.T., Girirajan, T.P.K. & Mason, M.D. Ultra-high resolution imaging by fluorescence photoactivation localization microscopy. *Biophys. J.* **91**, 4258–4272 (2006).
- Huang, B., Jones, S.A., Brandenburg, B. & Zhuang, X. Whole-cell 3D STORM reveals interactions between cellular structures with nanometer-scale resolution. *Nat. Methods* **5**, 1047–1052 (2008).
- York, A.G., Ghitani, A., Vaziri, A., Davidson, M.W. & Shroff, H. Confined activation and subdiffraction localization enables whole-cell PALM with genetically expressed probes. *Nat. Methods* **8**, 327–333 (2011).
- Cella Zanacchi, F. *et al.* Live-cell 3D super-resolution imaging in thick biological samples. *Nat. Methods* **8**, 1047–1049 (2011).
- Shroff, H., Galbraith, C.G., Galbraith, J.A. & Betzig, E. Live-cell photoactivated localization microscopy of nanoscale adhesion dynamics. *Nat. Methods* **5**, 417–423 (2008).

9. Jones, S.A., Shim, S.-H., He, J. & Zhuang, X. Fast, three-dimensional super-resolution imaging of live cells. *Nat. Methods* **8**, 499–508 (2011).
10. Hell, S.W. & Wichmann, J. Breaking the diffraction resolution limit by stimulated emission: stimulated-emission-depletion fluorescence microscopy. *Opt. Lett.* **19**, 780–782 (1994).
11. Donnert, G. *et al.* Macromolecular-scale resolution in biological fluorescence microscopy. *Proc. Natl. Acad. Sci. USA* **103**, 11440–11445 (2006).
12. Rankin, B.R. *et al.* Nanoscopy in a living multicellular organism expressing GFP. *Biophys. J.* **100**, L63–L65 (2011).
13. Berning, S., Willig, K.I., Steffens, H., Dibaj, P. & Hell, S.W. Nanoscopy in a living mouse brain. *Science* **335**, 551 (2012).
14. Gustafsson, M.G.L. Surpassing the lateral resolution limit by a factor of two using structured illumination microscopy. *J. Microsc.* **198**, 82–87 (2000).
15. Heintzmann, R. & Cremer, C. Laterally modulated excitation microscopy: improvement of resolution by using a diffraction grating. *Proc. SPIE* **3568**, 185–196 (1999).
16. Gustafsson, M.G.L. *et al.* Three-dimensional resolution doubling in wide-field fluorescence microscopy by structured illumination. *Biophys. J.* **94**, 4957–4970 (2008).
17. Kner, P., Chhun, B.B., Griffis, E.R., Winoto, L. & Gustafsson, M.G.L. Super-resolution video microscopy of live cells by structured illumination. *Nat. Methods* **6**, 339–342 (2009).
18. Shao, L., Kner, P., Rego, E.H. & Gustafsson, M.G.L. Super-resolution 3D microscopy of live whole cells using structured illumination. *Nat. Methods* **8**, 1044–1046 (2011).
19. Muller, C.B. & Enderlein, J. Image scanning microscopy. *Phys. Rev. Lett.* **104**, 198101 (2010).
20. Chitnis, A.B., Dalle Nogare, D. & Matsuda, M. Building the posterior lateral line system in zebrafish. *Dev. Neurobiol.* **72**, 234–255 (2011).
21. Aman, A. & Piotrowski, T. Wnt/ β -catenin and Fgf signaling control collective cell migration by restricting chemokine receptor expression. *Dev. Cell* **15**, 749–761 (2008).
22. Nechiporuk, A. & Raible, D.W. FGF-dependent mechanosensory organ patterning in zebrafish. *Science* **320**, 1774–1777 (2008).
23. Paszek, M.J. *et al.* Tensional homeostasis and the malignant phenotype. *Cancer Cell* **8**, 241–254 (2005).
24. Nelson, C.M. & Bissell, M.J. Of extracellular matrix, scaffolds, and signaling: tissue architecture regulates development, homeostasis, and cancer. *Annu. Rev. Cell Dev. Biol.* **22**, 287–309 (2006).
25. Engler, A.J., Sen, S., Sweeney, H.L. & Discher, D.E. Matrix elasticity directs stem cell lineage specification. *Cell* **126**, 677–689 (2006).
26. Pampaloni, F., Reynaud, E. & Stelzer, E.H.K. The third dimension bridges the gap between cell culture and live tissue. *Nat. Rev. Mol. Cell Biol.* **8**, 839–845 (2007).
27. Hasebe-Kishi, F. & Shimada, Y. Dynamics of actin and alpha-actinin in nascent myofibrils and stress fibers. *J. Muscle Res. Cell Motil.* **21**, 717–724 (2000).
28. Mattila, P. & Lappalainen, P. Filopodia: molecular architecture and cellular functions. *Nat. Rev. Mol. Cell Biol.* **9**, 446–454 (2008).
29. Grotjohann, T. *et al.* Diffraction-unlimited all-optical imaging and writing with a photochromic GFP. *Nature* **478**, 204–208 (2011).
30. Fiolka, R., Shao, L., Rego, E.H., Davidson, M.W. & Gustafsson, M.G.L. Time-lapse two-color 3D imaging of live cells with doubled resolution using structured illumination. *Proc. Natl. Acad. Sci. USA* **109**, 5311–5315 (2012).

ONLINE METHODS

Illumination system. All optics were mounted on an optical table (Kinetic Systems, Vibraplane model 5704-3660-23SPL) to minimize mechanical vibrations. For exciting fluorescence, two lasers were used: a 150-mW, 561-nm laser (561, Coherent, Sapphire 561-150 CW CDRH) and a 200-mW, 488-nm laser (488, Coherent, Sapphire 488-200 CDRH). Mechanical shutters (Thorlabs, SH05 and SC10) placed after each laser were used to control illumination. Beams were combined with a dichroic mirror (DC, Chroma, 525dcxru) and expanded 6.7× with a beam expander constructed from two achromatic lenses (Edmund, $f = 30$ mm, NT49-352-INK and Thorlabs, $f = 200$ mm, AC254-200-A-ML). Expanded beams were directed onto a DMD (Digital Light Innovations, D4100 DLP 0.55" XGA) 24 degrees off normal, so that in the 'on' position the micromirrors tilted the output beam normal to the DMD face. The central order of the resulting pattern was demagnified 1.5× with a beam de-expander (Thorlabs, $f = 75$ mm, AC254-075-A-ML and $f = 50$ mm, AC254-050-A-ML), aligned in a 4f configuration such that the DMD face was reimaged at the back focal plane of a 180 mm tube lens internal to the microscope (Olympus, IX81). These elements are shown in **Supplementary Figure 3**. After entering the left side port of the microscope, the beam sequentially passed through (i) the tube lens; (ii) a dichroic mirror (Chroma, zt405/488/561); (iii) a 60× objective (Olympus, PlanApo, NA 1.45 TIRE, for single fixed cells, or UPLSAPO 60XS, NA 1.3 silicone oil, for zebrafish, nematode and live cell samples) for a total demagnification of 90× between DMD and sample. The illumination at the sample covered a circular region ~50 μ m in diameter. For experiments with the 60× NA 1.45 objective, 488-nm power varied between 2.3 μ W and 25 μ W, and 561-nm power varied between 1.2 μ W and 15.2 μ W. For experiments with the 60×, NA 1.3 objective, 488-nm power varied between 2.5 μ W and 28.5 μ W, and 561-nm power between 1.4 μ W and 17 μ W. Power measurements were obtained at the output of the objective.

Microscope system. SIM imaging was performed on an Olympus IX81 inverted microscope equipped with left and right side ports, and an automated X-Y stage with an additional Z piezo-electric stage (200 μ m range, Applied Scientific Instrumentation, PZ-2000). The patterned excitation created by the DMD was brought into the microscope via the left side port. Fluorescence was collected by the objective, reflected with a dichroic (Chroma, zt405/488/561), passed through a 180-mm tube lens internal to the microscope, filtered appropriately to reject pump light (Semrock, LP02-488RE-25 and NF03-561E-25) and detected with an sCMOS camera (Cooke, pco.edge) mounted on the microscope right side port. Correctly aligning the sCMOS along the optical axis was critical in achieving near diffraction-limited performance. To aid in correct positioning of the camera, we replaced the 60× objectives typically used in imaging with a 10× air objective (Olympus, CPlanFl 10×, 0.3 NA), an optic much more sensitive to errors in axial alignment. We projected a fixed excitation pattern (similar to that used in SIM) onto FITC dye sandwiched between two glass coverslips ('fluorescent lake' sample) and translated the camera along the optical axis until the apparent size of each fluorescent spot was minimized.

Comparative confocal measurements. Point-scanned confocal images (**Supplementary Fig. 9**) were acquired using a [Zeiss](#)

[510 confocal microscope](#) and a 63× Plan-Apochromat (1.4 NA) oil objective. GFP was excited using a 488-nm laser and the emission was collected through a long-pass (LP) 505-nm filter. X-Y pixel sizes were set to achieve optimal theoretical optical resolution according to Nyquist criteria for the objective and excitation wavelength used. Interslice spacing for z stacks was set to 200 nm.

Fixed cellular samples. U2OS cells (a gift of M. Davidson, Florida State University) were cultured on ethanol-sterilized, cleaned (as described previously³¹) #1.5 25-mm-diameter cover slips (Warner Instruments, 64-0715) in standard growth medium (DMEM-HG (Invitrogen, 11960), sodium pyruvate (Invitrogen, 11360), GlutaMAX (Invitrogen, 35050) and 10% heat-inactivated FBS (Invitrogen, 11082)). To stain samples for microtubules, cells were fixed in a mixture of 0.5% glutaraldehyde, 0.37% formaldehyde and 0.3% Triton X-100 in cytoskeletal buffer (CB; 10 mM MOPS, 138 mM KCl, 3 mM MgCl₂, 2 mM EGTA, 0.01% NaN₃ and 160 mM sucrose, pH 6.1). After fixation, the cells were washed in CB, quenched with 100 mM glycine in CB, washed in CB and blocked in antibody-dilution buffer (AbDil buffer; 150 mM NaCl, 20 mM Tris, 0.1% Triton X-100, 0.1% NaN₃ and 2% bovine serum albumin, pH 7.4). The primary monoclonal antibody (Invitrogen, 32-2500) was diluted to 2 μ g/ml in AbDil buffer and incubated with the cells for 1 h at room temperature. After primary-antibody incubation, the cells were washed in phosphate-buffered saline before incubating them with the secondary, Alexa Fluor 488-labeled antibody (Invitrogen, A-11001) at 1:200 dilution in AbDil buffer for 1 h.

Samples for dual-color experiments (**Fig. 2**) were initially stained with Mitotracker Red (Invitrogen, M-7512) according to the manufacturer's instructions before fixation. After mitochondrial labeling, cells were fixed in 0.5% glutaraldehyde, 0.37% formaldehyde in CB, quenched in 100 mM glycine in CB and washed in CB. The antibody-labeling procedure outlined above was used to stain the microtubules. All samples were mounted in Fluoromount G (Electron Microscopy Solutions, 17984-25) to a standard 25 mm × 75 mm glass slide (SPI supplies, #01251-AB) and sealed with nail polish.

Live cellular samples. U2OS cells were cultured and transfected with plasmids expressing either GFP-myosin IIA or tdTomato-F-tractin³² via electroporation as previously described³³. A bottom layer of 3 mg/ml collagen I gel was assembled in MatTek dishes³⁴, using a sufficient volume to generate a 35–45- μ m-thick gel (confirmed by laser scanning confocal imaging of FITC-labeled collagen I). Cells were adhered to the top of the gel for 30–45 min, then encapsulated inside a 3D collagen gel by adding additional collagen on top of the cell layer. After adding media (McCoy's medium supplemented with 4 mM L-glutamine, 10% FBS, 10 mM HEPES pH 7.4), cells were imaged at 37 °C with an objective heater (Biopetechs, 150803 and 150819-13).

Subdiffractive beads. Yellow-green or red fluorescent beads (Invitrogen, F8803, 110 nm diameter; Invitrogen F8801, 100 nm diameter) were used for all PSF measurements. Beads were diluted from the stock concentration 1:1,300 (1:100 in distilled water and 1:13 in ethanol) and spread over cleaned glass cover slips. After air-drying for 5 min, to evaporate the ethanol, coverslips were

washed twice in distilled water to remove unattached beads. After air-drying again, beads were mounted in Fluoromount G (for deconvolving data sets displayed in **Figs. 1** and **2**) or silicone oil (for deconvolving data sets in **Figs. 3–5**) onto glass slides and sealed with nail polish.

Zebrafish samples. *Tg(XIEef1a1:dclk2-GFP)^{io008}* embryos carrying the zebrafish *dclk2-GFP* transgene were used in thick MSIM experiments (**Figs. 3** and **4**). To construct this line, plasmids containing the transgene were injected into one-cell zebrafish embryos along with *Tol2* mRNA. Fluorescent embryos were raised to adulthood and crossed to select for germline transmission by screening the offspring for GFP expression.

Tg(XIEef1a1:dclk2-GFP)^{io008} embryos were collected by natural spawning and maintained at 28 °C. Before MSIM, embryos at 24 h post-fertilization (h.p.f.) were anesthetized in Tricaine (Sigma, E10521) at a final concentration of 600 µM in embryo medium (60 mg RedSea Coral Pro Salt (Drs Foster and Smith Pet Supplies) per liter ddH₂O). Anesthetized embryos were mounted on round coverslips, immobilized in 1% low-melt agarose (Cambrex, 50080), placed in a round coverslip holder (ASI, I-3033-25D), covered with embryo medium and imaged at room temperature.

Worm samples. Strain BV24 (*ltIs44 [pie-1p-mCherry::PH(PLC1delta1) + unc-119(+)]*; *zuIs178 [(his-72 1kb::HIS-72::GFP); unc-119(+)]* V; gift of Z. Bao) was raised at 20 °C on NGM medium seeded with *Escherichia coli* OP50. Gravid worms were picked from the plate, placed into methyl cellulose and cut in half to release embryos. Embryos were subsequently transferred to cleaned cover slips, placed in the same holder used for zebrafish experiments, covered with silicone oil (Olympus, Z-81114) and imaged at room temperature. Under these conditions, embryos did not develop past the L1 larvae stage.

Tg(XIEef1a1:dclk2-GFP)^{io008} embryos were collected by natural spawning and maintained at 28 °C. For live imaging, embryos at 24 h.p.f. were anesthetized in Tricaine at a final concentration of 600 µM in standard embryo media. Anesthetized embryos were immobilized in 1% low-melt agarose and mounted laterally on glass cover slips. The coverslip was mounted in a custom chamber, and embryos were covered in embryo medium with Tricaine.

Data acquisition. Before image acquisition, the onboard memory of the DMD was preloaded with our multifocal illumination patterns. The DMD displayed the patterns in sequence, sending transistor–transistor logic (TTL) pulses to the camera to trigger exposures. The DMD ‘trigger out’ signal was high during pattern exposure, and low during the ‘off’ state. We set the DMD to expose each illumination pattern for 2.2 ms, then turned every pixel off for 2.3 ms. We set the camera to expose for 2.2 ms every time it received a trigger pulse. These timing settings enabled

the maximum frame rate for a 480 × 480 pixel field of view (4.5 ms/frame or 222 frames/s) and synchronized illumination and exposure to give the highest signal for a given light dose to the sample. Additional details are available in **Supplementary Notes 2** and **3**.

Data processing. After acquisition, we processed each set of raw images into a super-resolution image using custom software written in the Python programming language³⁵. The processing steps were: (i) automatic lattice detection, to determine the locations of the illumination spots precisely; (ii) digital pinhole masking around each detected illumination spot to reject out-of-focus light and optional flat-fielding using calibration data; (iii) local contraction (scaling), resampling the area around each illumination spot to improve the resolution by $\sqrt{2}$; (iv) summing the processed images to produce an MPSS image; (v) using deconvolution to recover the full 2× resolution enhancement. MPSS methods are described in detail in **Supplementary Note 4**, and our open-source processing code is available at <http://code.google.com/p/msim/>. The version of the software used to generate the results reported in this manuscript is available in **Supplementary Software**.

Deconvolution. MPSS data sets were deconvolved using P. Wendykier’s Parallel Iterative Deconvolution plugin for ImageJ (freely available at <http://sites.google.com/site/piotrwendykier/software/deconvolution/paralleliterativedeconvolution>). Experimentally measured PSFs (MPSS images of beads, derived either from 110-nm yellow-green beads or 100-nm red beads) were used for 3D deconvolution. For all deconvolution operations, we used the following parameters: Method, Wiener Filter Preconditioned Landweber³⁶; Preconditioner, FFT Preconditioner; Tolerance, 0.0; Boundary, Reflexive; Resizing, Auto; Output, Float; Precision, Double; Max number of iterations, 100. On all our data sets, deconvolution converged in <50 iterations.

31. Shroff, H. *et al.* Dual-color superresolution imaging of genetically expressed probes within individual adhesion complexes. *Proc. Natl. Acad. Sci. USA* **104**, 20308–20313 (2007).
32. Yi, J., Wu, X., Crites, T. & Hammer, J.A. III. Actin retrograde flow and acto-myosin II Arc contraction drive receptor cluster dynamics at the immunological synapse in Jurkat T-cells. *Mol. Biol. Cell* **23**, 834–852 (2012).
33. Pasapera, A., Schneider, I., Rericha, E., Schlaepfer, D. & Waterman, C. Myosin II activity regulates vinculin recruitment to focal adhesions through FAK-mediated paxillin phosphorylation. *J. Cell Biol.* **188**, 877–890 (2010).
34. Fischer, R., Gardel, M., Ma, X., Adelstein, R. & Waterman, C. Local cortical tension by myosin II guides 3D endothelial cell branching. *Curr. Biol.* **19**, 260–265 (2009).
35. Oliphant, T. Python for scientific computing. *Comput. Sci. Eng.* **9**, 10–20 (2007).
36. Dougherty, R.P. Extensions of DAMAS and benefits and limitations of deconvolution in beamforming. *AIAA Pap.* 1–13 (2005).